



Article

The Kinetics of Aragonite Formation from Solution via Amorphous Calcium Carbonate

Simon M. Clark ^{1,2,*}, Vili Grigorova ¹, Bruno Colas ^{1,2}, Tamim A. Darwish ³, Kathleen Wood ², Joerg Neufeind ⁴ and Dorrit E. Jacob ⁵

¹ School of Engineering, Faculty of Science and Engineering, Macquarie University, North Macquarie Park, Shellharbour, NSW 2109, Australia

² Australian Centre for Neutron Scattering, Australian Nuclear Science and Technology Organisation, Locked Bag 2001, Kirrawee DC, Sydney, NSW 2232, Australia

³ National Deuteration Facility, Australian Nuclear Science and Technology Organisation, Kirrawee DC, Sydney, NSW 2232, Australia

⁴ Spallation Neutron Source, Oak Ridge National Laboratory, Oak Ridge, TN 37831, USA

⁵ Research School of Earth Sciences, The Australian National University, Canberra, ACT 2600, Australia

* Correspondence: simon.clark@mq.edu.au

Abstract: Magnesium doped Amorphous Calcium Carbonate was synthesised from precursor solutions containing varying amounts of calcium, magnesium, H₂O and D₂O. The Mg/Ca ratio in the resultant Amorphous Calcium Carbonate was found to vary linearly with the Mg/Ca ratio in the precursor solution. All samples crystallised as aragonite. No Mg was found in the final aragonite crystals. Changes in the Mg to Ca ratio were found to only marginally effect nucleation rates but strongly effect crystal growth rates. These results are consistent with a dissolution-precipitation model for aragonite formation via an Amorphous Calcium Carbonate intermediate.

Keywords: neutron scattering; X-ray diffraction; Small Angle Neutron Scattering; Laser-Ablation Inductively Coupled Plasma Mass Spectrometry; thermo gravimetric analysis; NOMAD; QUOKKA; ACC; aragonite; Mg/Ca



Citation: Clark, S.M.; Grigorova, V.; Colas, B.; Darwish, T.A.; Wood, K.; Neufeind, J.; Jacob, D.E. The Kinetics of Aragonite Formation from Solution via Amorphous Calcium Carbonate. *Nanomaterials* **2022**, *12*, 4151. <https://doi.org/10.3390/nano12234151>

Academic Editor: Rodolphe Antoine

Received: 14 October 2022

Accepted: 21 November 2022

Published: 23 November 2022

Publisher's Note: MDPI stays neutral with regard to jurisdictional claims in published maps and institutional affiliations.



Copyright: © 2022 by the authors. Licensee MDPI, Basel, Switzerland. This article is an open access article distributed under the terms and conditions of the Creative Commons Attribution (CC BY) license (<https://creativecommons.org/licenses/by/4.0/>).

1. Introduction

Amorphous calcium carbonate (ACC) plays a key role in the early stages of biomineralisation as a precursor to crystalline calcium carbonate phases (e.g., [1]) and is a model system in the development of biomimetic materials. Many organisms take advantage of the mouldable character of ACC in the formation of their intricate shells and skeletons. ACC also seems to lower the activation energy for nucleation of subsequent crystalline carbonates due to lower surface energies [2] enabling an ambient temperature non-classical crystallisation pathway [3]. It is known that ACC is polyamorphous with different water content, local order and mode of formation [4,5], and it was recently shown that ACC is best described as a nano-fluid [6]. Understanding the mechanism by which these nanoparticles self-assemble is essential if we are to understand the effect of climate change on marine life and how well we are presently using the fossil record to constrain climate change models.

In the laboratory ACC converts to the crystalline carbonate phases in a matter of minutes although, depending on the aqueous fluid composition and any additives [7], its stability can be increased allowing ACC to be preserved for weeks to years [8,9]. The additives most commonly used in the laboratory to prolong ACC lifetime are organic macromolecules, such as polyacrylic acid [10,11] and magnesium [11–14]. In natural biominerals, in addition to Mg, a large range of organic macromolecules can exert a stabilising effect on ACC, which can extend the stability of ACC almost indefinitely [15]. Mg-ACC usually transforms into calcite at low Mg content [16–19], but at high Mg content transforms into aragonite [17,18].

Non-classical nucleation and growth models often provide a better description of biomineralization kinetic data than classical crystallisation models [3]. In this context, two models have been used to describe the transformation mechanism from ACC to aragonite or calcite in non-classical crystallisation: a solid-state transformation, where ACC dehydrates and crystallises into a calcium carbonate polymorph directly in the solid phase [1,20]; or a dissolution-reprecipitation process [20–22], where ACC dissolves and crystalline calcium carbonate precipitates from this solution. In the laboratory, ACC usually transforms via dissolution precipitation which is typically associated with significant morphological changes to the texture of the solid phase [20,23,24]. In vivo, preservation of intricate hierarchical structural details [25] during stepwise crystallisation seems to contradict the findings in the laboratory, but supports either solid-state transformation, or very localised dissolution-reprecipitation processes or perhaps a combination of both [23,26].

To try to distinguish between these two models, we measured the rate of formation of crystalline aragonite from ACC in the laboratory for a range of Mg/Ca ratio and H₂O/D₂O compositions.

2. Methodology

2.1. Sample Preparation

A set of ACC samples with a range of Mg/Ca ratios and water contents were synthesised with Mg/Ca ratios expected to give measurable formation and crystallisation rates. A commonly used synthesis procedure was followed [27] and modified with or without an additional freeze-drying step to allow variation of water content. Stock 0.02 M solutions of Na₂CO₃ and 0.02 M solutions made by dissolving various mixtures of solid CaCl₂ and MgCl₂ in water or heavy water to give solutions with a range of Mg/Ca content, were prepared and stored at 4 °C. About 100 mL of both the stock Na₂CO₃ and CaCl₂/MgCl₂ solutions were then quickly mixed together in a 250 mL bottle held at 4°C while stirring using with a magnetic stirrer. Almost instantly the solutions were mixed a white precipitate formed. The white precipitate was filtered and washed with acetone and then either stored under nitrogen at room temperature or freeze-dried for one hour before being stored under nitrogen at room temperature. Stock solutions were prepared using H₂O, D₂O and mixtures of H₂O and D₂O as the solvent in order to vary the solvent chemistry and probe the effect of solvent on sample structure, stability, and crystallisation products.

2.2. Analysis Techniques

Each ACC sample synthesised was characterised using Thermal Gravimetric Analysis (TGA), to determine the amount of water present, Laser-Ablation Inductively Coupled Plasma Mass Spectrometry (LA-ICPMS), to determine the Mg/Ca ratio, Neutron scattering to confirm the LA-ICPMS measurements, and X-ray diffraction (XRD) to confirm that there were no crystalline phases present in the sample. Each of the carbonates crystallised from our ACC samples were characterised using Raman Spectrometry and powder X-ray Diffraction to determine which calcium carbonate polymorph was present, Scanning Electron Microscopy to provide visual evidence of sample composition, and a second powder X-ray diffraction measurement incorporating an internal standard to provide accurate crystalline phase lattice parameters. Finally, time resolved Small Angle Neutron Scattering (SANS) was used to measure the rate of formation of ACC from solution, and time resolved powder X-ray diffraction was used to determine the rate of formation of crystalline carbonate phases upon transformation of the ACC samples.

The TGA measurements utilised a TA Instruments TGA 2050. The sample temperature was increased from 20 °C to 800 °C, at a rate of 10 °C/min in a N₂ atmosphere while measuring the weight of the sample. For the LA-ICPMS we used a Photon Machines G2 Excimer laser system (wavelength 193 nm) coupled with an Agilent 7700 quadrupole ICP-MS. ACC samples were dried at 100 °C for 36 h, pressed into pellets and measured with laser spot size of 50 µm and pulse rates of 5 Hz (energy density 5.42 J/cm²). Backgrounds were measured for 30 s followed by 40 s of sample ablation. NIST SRM (US National Institute of

Standard and Technology Standard Reference Material) 610 glass was used as the external standard with ^{43}Ca as the internal standard. The mg for NIST SRM 610 reported in the GeoReM database was used as the “true” concentration in this reference glass [28]. Neutron scattering data were collected using the NOMAD instrument at the Spallation Neutron Source, Oak Ridge National Laboratory, USA. Samples synthesized using 100% D_2O to reduce background noise from inelastic scattering of neutrons from protons, were loaded into 5 mm diameter quartz capillary tubes inside a glove box under a nitrogen atmosphere, sealed and quickly transported to the instrument. Scattering data were collected in 30 min frames at room temperature in an argon atmosphere for a total of 1.5 h. The standard instrument data reduction software was used to normalize the data and for background subtraction. XRD patterns were collected using a PANalytical Expert Pro MPD (Multi-Purpose Diffractometer) with a Copper tube (45 kV, 40 mA), Soller slits (0.04 rad.) and fixed incident beam mask (15 mm). The instrument zero point was calibrated using the NIST 640c Si standard. The samples were placed on zero background sample holders, and the wavelength used was $\text{CuK}\alpha$ ($\lambda = 1.54 \text{ \AA}$). For the accurate lattice parameter measurements appropriate amounts of the NIST, Silicon Powder, Standard Reference Material[®] 640c was mixed with each sample to increase the accuracy of the measurement. Unit cell parameters were then determined using the Profex software package [29]. Series of powder XRD patterns were also collected from ACC samples using the same system at ambient temperature while they transformed into crystalline carbonate phases. Diffraction patterns were collected over the 10° to 50° 2θ range every 30 min for 24 to 48 h for a range of initial conditions. Peak intensities were determined from these spectra as a function of time and converted into a measure of the degree of reaction for subsequent analysis. Raman spectra were collected using a Horiba LABRAM HR Evolution confocal laser Raman spectrometer. The spectrometer used a red excitation laser ($\lambda = 633 \text{ nm}$) and a 1800 gr/mm grating. Before collecting data from each sample, the spectrometer was calibrated using the Rayleigh line and a Si-wafer with a sharp peak at 520 cm^{-1} . A JEOL JSM- 6480 LA Scanning Electron Microscope (SEM) was used to obtain SEM micrographs from gold coated samples. SANS data were collected using the QUOKKA instrument [30] at the Australian Centre for Neutron Scattering, Australian Nuclear Science and Technology Organisation, Lucas Heights, Australia. Samples were placed in quartz Hellma cells mounted in a thermally controlled sample changer. The neutron path length through the sample was 2 mm and the cell volume $600 \mu\text{L}$. For each measurement, the solutions made from Na_2CO_3 , CaCl_2 and MgCl_2 were mixed in the cells minimising any lag between mixing and the start of data collection. All solutions were made with only D_2O , because samples with H_2O were found to give too large a background signal due to incoherent scattering from protons. The source was set to a wavelength of $\lambda = 5 \text{ \AA}$, and the detector placed 8 m from the sample. Samples with Mg/Ca ratios of 0.03, 0.2 and 0.26 were studied at ambient temperature to simulate in vivo conditions as closely as possible.

3. Results

3.1. Characterisation of the Amorphous Phase

The main aims of the ACC characterisation were to check that the samples had not transformed to a crystalline carbonate phase, to determine the Mg/Ca ratios and the amount of water.

3.1.1. Thermal Gravimetric Analysis

A typical TGA pattern is shown in Supplementary Materials Figure S1. The weight loss at around 100°C was attributed to loss of surface water, the small weight loss around 350°C was attributed to the loss of included water and the weight loss around 700°C was attributed to the loss of carbon dioxide in keeping with previous studies [16,19]. The stoichiometric water loss was calculated from this weight loss assuming a sample formula of $(\text{Ca}_{1-x}\text{Mg}_x)\text{CO}_3 \cdot n\text{H}_2\text{O}$. The results are summarised in Supplementary Material Table S1. Freeze-dried samples were found to contain about 1.18 molecules of water per formula

unit, and filtered samples were found to contain about 2.69 molecules of water. This was independent of the Mg/Ca ratio or whether the solvent contained H₂O, D₂O or a mixture of the two (Supplementary Materials Table S1). These values are comparable with those found previously, such as $n = 1.42\text{--}1.63$ [19], and $n = 0.98\text{--}1.4$ [16]. Freeze drying can be seen to have the effect of reducing the amount of water percent in an ACC sample.

3.1.2. X-ray Diffraction

XRD patterns of the freshly synthesised ACC samples were found to contain no Bragg peaks. We observed only broad humps indicative of an amorphous or nano-crystalline phase with two diffuse maxima at 32° ($d = 2.8$ Å) and 46° ($d = 2.0$ Å) 2θ (Supplementary Figure S2) consistent with those previously measured from ACC samples [16].

3.1.3. Laser-Ablation Inductively Coupled Plasma Mass Spectrometry

Representative measured Mg/Ca values are contained in Supplementary Materials Table S1. In Figure 1 the Mg/Ca ratios determined using LA-ICPMS are plotted against the Mg/Ca ratios of the solutions from which the ACC samples formed. Comparing data from this study (blue spots) with data from other studies [23,30–33] (Figure 1) shows a linear correlation with the Mg/Ca ratio in solution, with an apparent distribution coefficient ($K_d = [(Mg/Ca)_{ACC}/(Mg/Ca)_{solution}]$) of 0.12. The exact relationship seems to be highly dependent upon the reported study with our data in the same range as data from two previous measurements [23,34]. Further reference to Mg/Ca ratios in this manuscript will refer to the Mg/Ca ratio of the solid sample and not the nascent solution. Potentially, the measured Mg/Ca ratio in the solid sample could be due to variations in the washing and drying protocols with some measurement signal coming from fluid still adhering to solid particles. To investigate this possibility, we also used neutron scattering to determine Mg/Ca ratios.

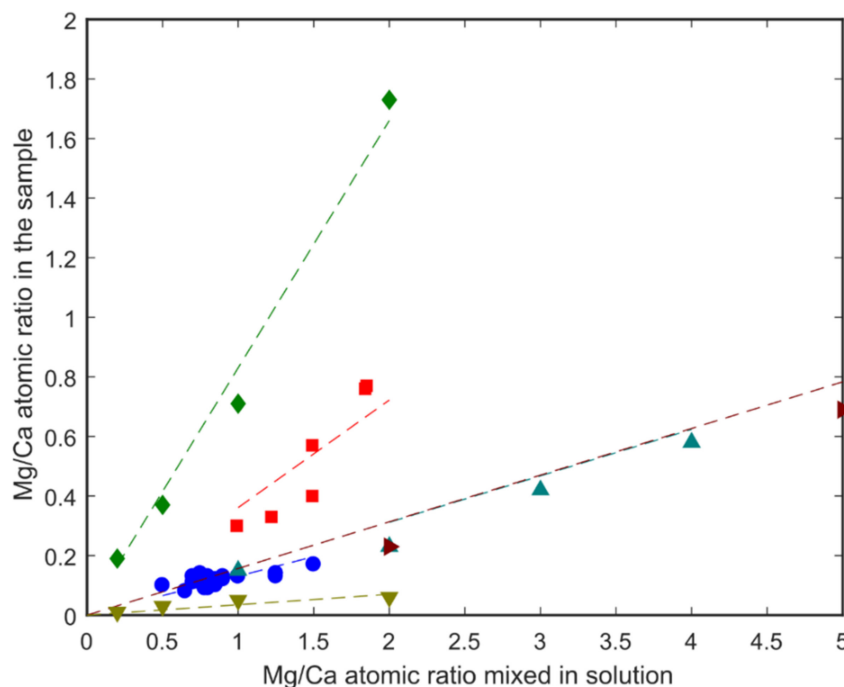


Figure 1. Comparison of Mg/Ca ratios measured in ACC samples to Mg/Ca ratios of the solutions from which they formed for samples: ● from this study, ◆ mixed with Formamide [33], ■ [31], ▲ [32], ► [23], ▼ with water [33]; the dashed lines are linear fits to the data points of corresponding colour.

3.1.4. Neutron Scattering

A previous study showed that scattering from an ACC sample containing only Ca has a peak in the real space scattering intensity at $G(r) \approx 2.3 \text{ \AA}$, due to Ca-O correlations. In comparison, an ACC sample containing only Mg has a peak in the real space scattering intensity at $G(r) \approx 2.1 \text{ \AA}$. ACC samples with mixtures of Ca and Mg have both peaks with the positions of these peaks varying linearly between the two solid solution end members (Supplementary Material Figure S3). This provides a methodology for the measurement of Mg/Ca ratio in an ACC sample free from any remnant liquid phase contamination. Neutron scattering patterns of six samples containing different Mg/Ca proportions, x , given by the general formula: $(\text{Ca}_{1-x}\text{Mg}_x)\text{CO}_3 \cdot n\text{H}_2\text{O}$, are shown in Supplementary Material Figure S4. The sample with Ca only contains one peak at $\sim 2.4 \text{ \AA}$ due to Ca-O correlations, while the samples made from mixtures of Mg and Ca contain peaks at $\sim 2.2 \text{ \AA}$ and $\sim 2.4 \text{ \AA}$ due to Mg-O and Ca-O correlations, respectively. This observation demonstrates that Mg is indeed incorporated in the ACC atomic structure and is not a measurement artefact.

The positions of these two peaks are presented in Figure 2 as a function of Mg/Ca ratio together with data from a previous study [31]. The two datasets are seen to be well correlated. The peak due to Ca-O correlations at $\sim 2.4 \text{ \AA}$ does not change with Mg/Ca ratio while the peak due to Mg-O correlations is seen to vary from $\sim 2.2 \text{ \AA}$ at low Mg content to $\sim 2.1 \text{ \AA}$ at 100% Mg content. These data confirm that the LA-ICPMS measurements provide an accurate determination of the Mg/Ca ratios in our samples. The data also demonstrate that comparison of the positions of the Ca-O and Mg-O correlation peaks from neutron scattering data provides an accurate method for the determination of Mg/Ca ratios with no need for any calibrations using standards.

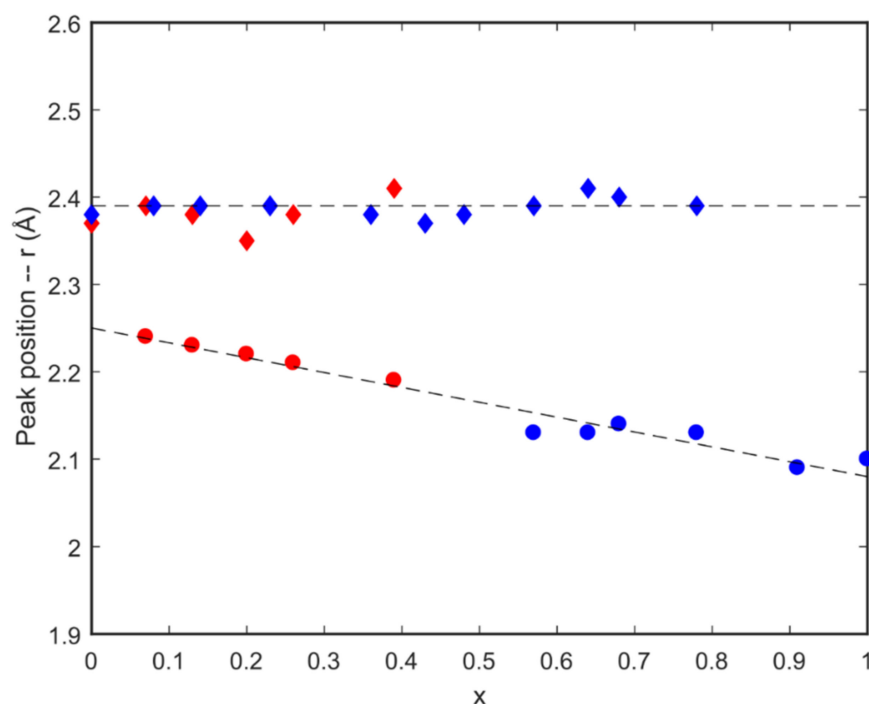


Figure 2. Peak positions of the first Mg-O and Ca-O correlations, taken from Supplementary Materials Figures S3 and S4, Where x is the proportion of magnesium in the sample as given by: $(\text{Ca}_{1-x}\text{Mg}_x)\text{CO}_3$. The data shown as red markers are from this study (Figure S4), and the blue markers from [31] (Figure S3). Filled diamond symbols denote the first Ca-O correlation peak around 2.4 \AA ; Filled circle symbols denote the first Mg-O correlation peak around $2.1\text{--}2.2 \text{ \AA}$.

The background intensity of the neutron scattering patterns can be used to estimate the H₂O/D₂O ratios in our samples by use of a calibration curve made from known pure H₂O/D₂O mixtures (Supplementary Materials Figure S5). This leads us to conclude that there is less than 10% H₂O in our fully deuterated samples and, thus, more than 90% D₂O. This provides an error estimate for our determined H₂O/D₂O ratios of about 5% due to contamination related to the highly hygroscopic nature of D₂O. It translates into an uncertainty in the number of water molecules per formula unit of about ± 0.06 for the freeze-dried samples and ± 0.13 for the filtered samples. Comparing these uncertainties with the range of measured values using TGA of 0.9 to 1.37 for the freeze-dried samples and 2.12 to 3.46 for the filtered samples, it implies that the effect of freeze-drying vs. filtering is negligible.

3.2. Characterisation of the Crystalline Phases

The main aim of the characterisation of the crystalline phases was to determine which carbonate polytypes formed and their Mg/Ca ratios.

3.2.1. Raman Spectroscopy

Raman spectra collected from our samples were compared to spectra we collected from reference samples of pure aragonite and calcite (Supplementary Materials Figure S6). Comparison of these spectra showed that the crystallised sample consisted solely of aragonite. This was confirmed by comparison with reference data from [35,36] and the RRUFFTM database [37]. The spectra were found to contain three peak groupings: the ν_1 symmetric stretching of the carbonate groups at 1085 cm⁻¹; the ν_4 in-plane bending of calcite at 711 cm⁻¹, and the ν_4 in-plane bending of aragonite at 706 cm⁻¹ and 701 cm⁻¹ and the lattice modes of calcite at 155 cm⁻¹ and 281 cm⁻¹, and the lattice modes of aragonite at 206 cm⁻¹ and 155 cm⁻¹. All crystallised samples measured consisted solely of the aragonite phase.

3.2.2. X-ray Diffraction

XRD patterns from the crystalline phases produced from our ACC samples were fitted using the *Profex* (Solothurn, Switzerland) software [29] and were found to contain only reflections due to aragonite (Supplementary Materials Figure S7) showing that only aragonite crystals formed in agreement with our Raman data.

3.2.3. Scanning Electron Microscopy

A representative SEM image is contained in the Supplement Materials Figure S5. Clusters of tablet-shaped aragonite crystals can be seen. These are surrounded by xenomorphic, rounded grains that we interpret as ACC particles. The aragonite tablets are of similar size and shape as ones observed in nacre, 0.5 μm thick, 5–15 μm in diameter polygons [38]. This supports the conclusions of both Raman and XRD measurements that only aragonite is present in the crystallised samples.

3.2.4. High-Precision X-ray Diffraction

Accurate determination of the Mg/Ca ratio in carbonates crystallised from ACC is difficult due to the presence of ACC particles on crystal faces (Supplementary Figure S8) and in between the carbonate platelets making up the crystalline phase. The unit cell volume of carbonate phases is highly sensitive to any incorporation of other ions such as magnesium and should prove an accurate method for determining the Mg/Ca ratio. The unit cell volume of aragonite crystallised from our ACC as a function of Mg/Ca ratio in the precursor ACC is shown in Figure 3. The volume is seen to show only a small change from the volume of pure calcium containing aragonite with Mg/Ca ratio. How significant this small change is in the absence of literature aragonite unit cell volume data for varying Mg/Ca ratios can be estimated by comparison of volume change with substitution of other similar atoms. Volumes calculated for substitution of Ca by Sr in the aragonite

(CaCO₃) to strontianite (SrCO₃) solid solution series [39] are also plotted in Figure 3. It was observed that there is an increase in unit cell volume with increasing amounts of Sr which is probably due to the Sr atom being bigger (in a crystal 1.32 Å) than a Ca atom (1.14 Å). In a similar manner, the unit cell volume of aragonite on substitution of calcium (1.14 Å) with magnesium (0.86 Å) was calculated the result of which is also plotted in Figure 3. Our conclusion is that there is no significant substitution of calcium by magnesium in the crystalline aragonite samples although it was previously incorporated in the ACC before transformation to aragonite.

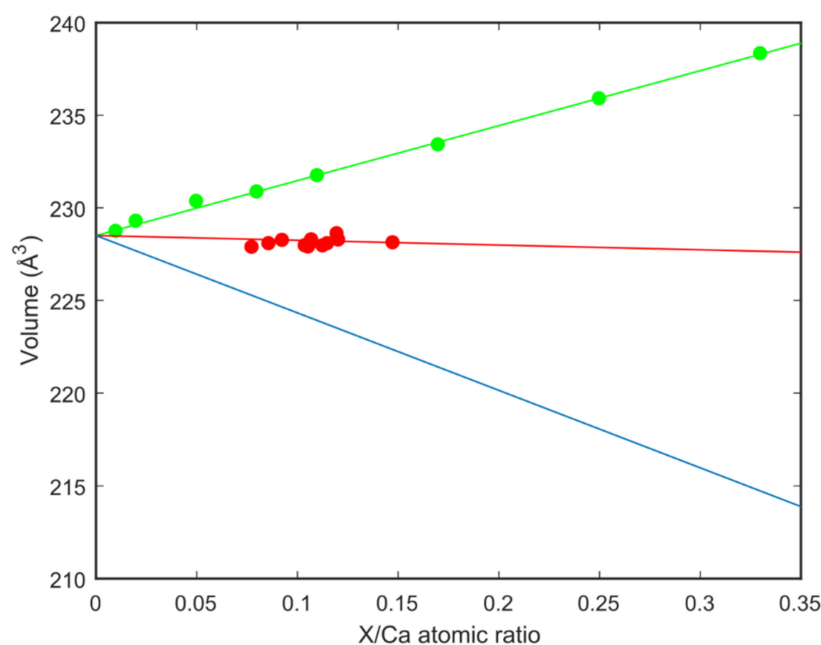


Figure 3. Data from this study compared to the unit cell volume change of the lattice estimated for substitution of Sr and Mg to Ca. X represents either Sr or Mg. ● Data from this study with the linear fit of the data points; ● Strontianite (SrCO₃)-aragonite (CaCO₃) solid solutions from [39] with the linear fit of the data points; — Estimate for Mg substituting Ca in the aragonite.

3.3. Kinetics of Particle Growth and Crystallisation of Calcium Carbonate

SANS is the most suitable method for measuring the kinetics of ACC formation given the previously observed length scales of ACC particles. For determining the kinetics of aragonite formation time resolved powder X-ray diffraction is more appropriate given the crystalline nature of the product phase.

3.3.1. Small-Angle Neutron Scattering

A time resolved SANS measurement determines scattering intensity as a function of momentum transfer for particles of nanometre to micro size in a series of time slices. The shape and slope of each of these scattering curves depends on the size and shape of the particles in the sample. A typical series of SANS spectra collected during the formation of one of our ACC samples is shown in Supplementary Materials Figure S9 together with the extracted degree of formation curve and determined rate values. The data were fitted with two models; the first one was a simple spherical particle model, that considers all particles to be spheres and fits the radius to the data; and a Porod-Guinier model, that has a shape parameter as well as a size parameter using the SasView software package [40]. Both models gave similar results consistent with a spherical particle shape. ACC particles were found to start with an average radius of around 35 nm which grew to around 60 nm after 4–5 h for the samples with Mg/Ca ratios of 0.03 and 0.2. ACC particles with a Mg/Ca ratio of 0.26 also started with a radius of about 35 nm which remained constant for the duration of the measurement. A summary of particle size evolution under varying conditions is

shown in Figure 4. The height of the peak in the SANS patterns was used to estimate the amount of ACC particles of each size as a function of time. These data were then fit with the Avrami equation [5]. This gave an estimate of the rate of formation of the initial 35 nm particles (rate = 0.17 h⁻¹ for a Mg/Ca ratio of 0.26, rate = 0.27 h⁻¹ for a Mg/Ca ratio of 0.2 and rate = 0.3 h⁻¹ for a Mg/Ca ratio of 0.03) and the rate of transformation from 35 to 60 nm particles (rate = 2.8 h⁻¹ for a Mg/Ca ratio of 0.03 and rate = 0.9 h⁻¹ for a Mg/Ca ratio of 0.2 (Figure 5). The Mg/Ca ratio of 0.26 sample did not show any growth during the measurement period.

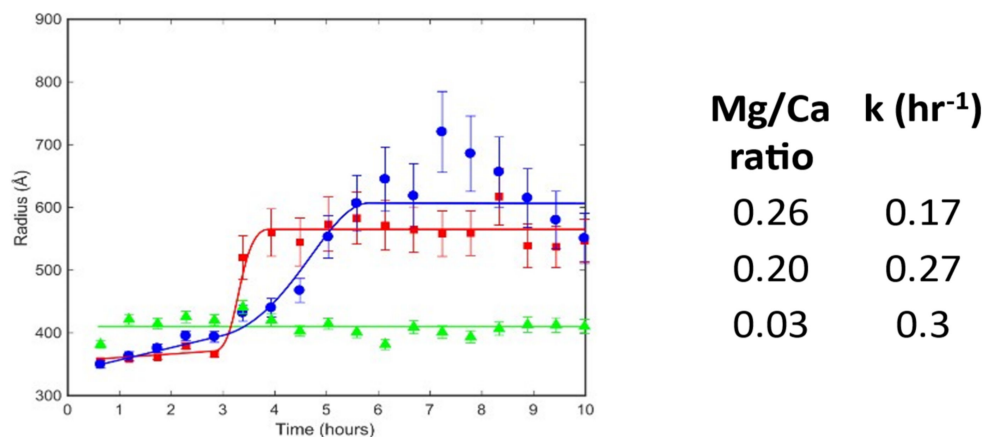


Figure 4. Evolution of the particle size in the samples analysed at 20 °C (ambient) with time. ▲ is for the sample with Mg/Ca = 0.26; ● is for the sample with Mg/Ca = 0.20; and ■ is for the sample with Mg/Ca = 0.03. The corresponding lines are guides for the eye. The table contains estimates of the rate of transformation between the 35 nm and nm particles for three Mg/Ca ratios.

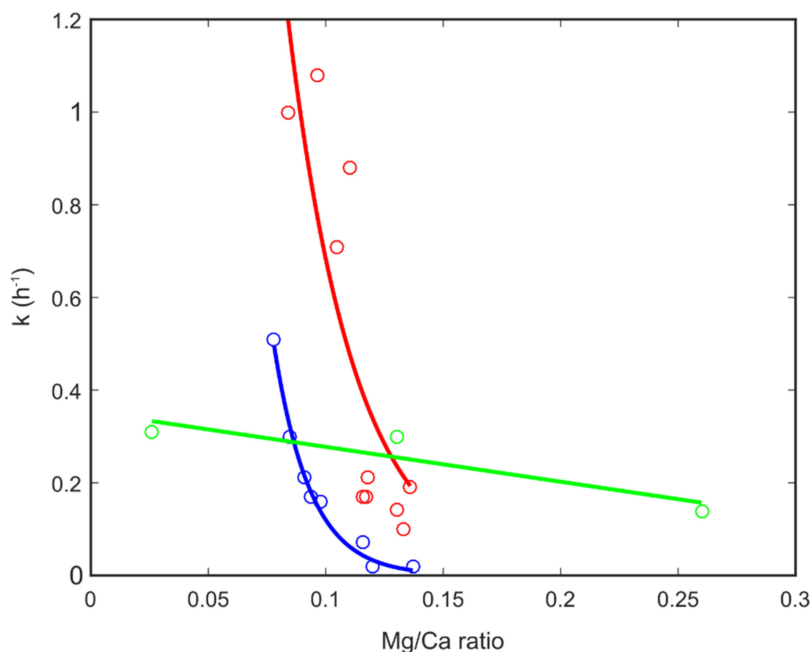


Figure 5. Reaction rates for the formation of initial ACC particles (green symbols and line) and subsequent formation of aragonite crystals (red symbols and line for formation in H₂O and blue symbols and lines formation in D₂O). The red and blue lines are exponential fits to the corresponding symbols, their equations are $y = 22.87 e^{-35.11 x}$ for the red line and $y = 76.38 e^{-64.57 x}$ for the blue line. The green line is a linear fit to the corresponding symbols giving: $y = -0.75 x + 0.35$.

3.3.2. X-ray Diffraction

A representative series of powder diffraction patterns are presented in Supplementary Materials Figure S10. The aragonite (111) and (221) peaks are seen to grow out of the background due to nano-crystalline calcium carbonate. The intensity of the (111) peaks were used to determine the degree of reaction for each series of XRD patterns which was then used with the Avrami equation [5] to give the corresponding reaction rate Figure 6). Broad amorphous scattering was observed but no sharp diffraction signal from a crystalline product within the time frame of our measurements when the ACC precursor had an Mg/Ca ratio of above about 0.14. Some samples with very high Mg/Ca ratios were found to be still amorphous many months after they were synthesised.

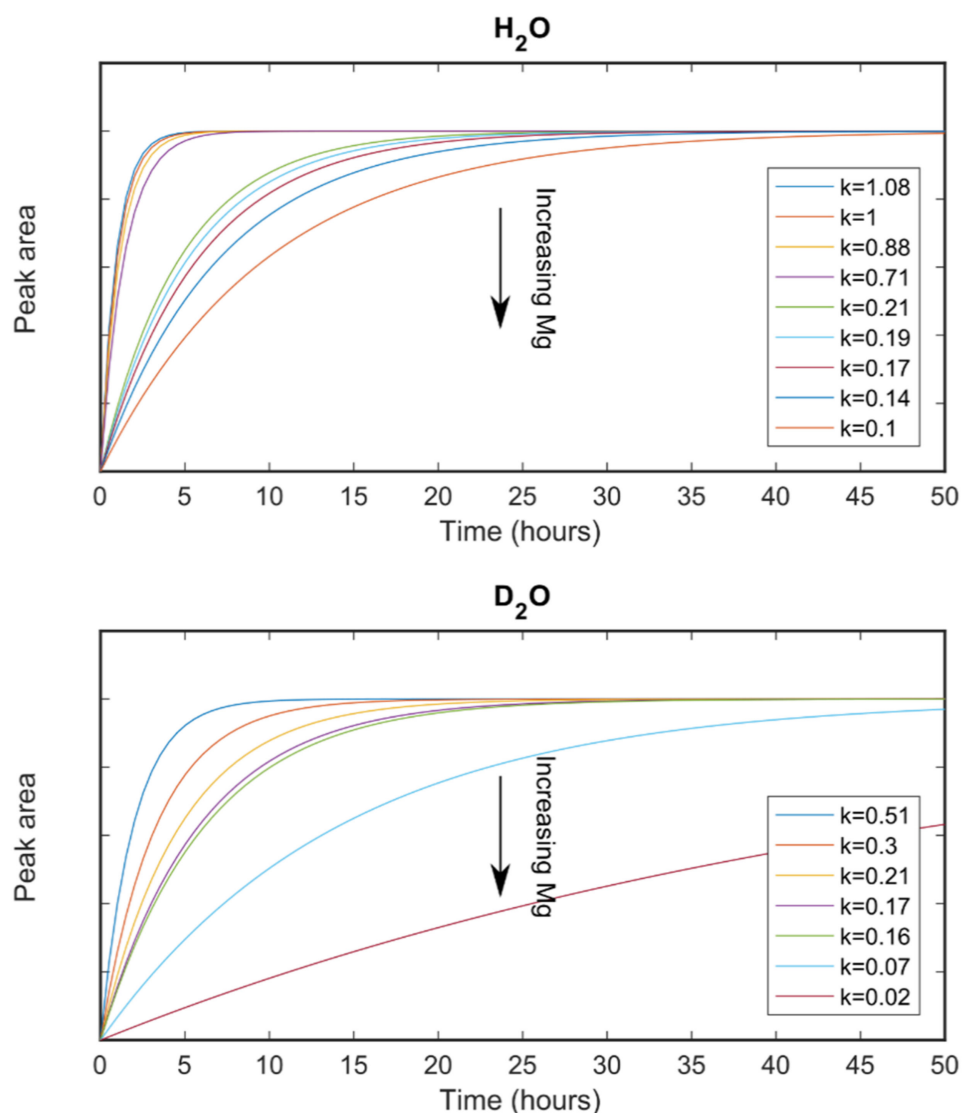


Figure 6. Compilation of the degree of aragonite formation as a function of magnesium content for samples formed from ACC with varying Mg/Ca ratios using H₂O and D₂O as the solvent.

4. Discussion and Conclusions

All samples of ACC synthesised during this study crystallised into aragonite as confirmed by XRD and Raman data. After the completion of crystallisation, a small amount of remnant ACC particles were observed on aragonite crystals, consistent with observations in natural systems such as mollusc shells [41,42]. Mg was found to be present in the nano-crystalline ACC atomic structure but not in the crystalline aragonite atomic structure. This suggests that Mg was lost during the transformation of ACC into aragonite. The lost Mg

atoms most likely were incorporated into the remnant ACC particles observed on the surface of the aragonite crystals in our SEM images, stabilising this portion of the ACC to allow it to exist for extended periods of time as observed in ACC cortices around crystalline nacre tablets in mollusc shells [43,44].

The redistribution of Mg upon transformation of ACC into aragonite observed here requires transport of ions from the ACC nano-particles forming the crystalline phase, and thus, is consistent with a dissolution-reprecipitation process and discounts a pathway of solid-state transformation [3]. A schematic representation of the transformation process from solution through ACC to crystalline aragonite consistent with the data collected in this work is contained in Figure 7. We observe three steps:

1. Precipitation of ACC from solution forming 35 nm particles: reaction R_1 .
2. The 35 nm particles grow into 70 nm particles: reaction R_2 .
3. Formation of aragonite crystals by localised dissolution and reprecipitation: reaction R_3 .

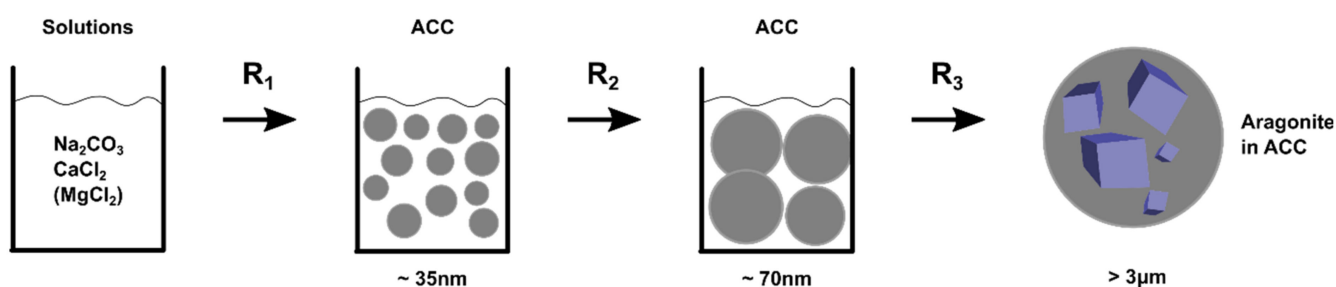


Figure 7. Schematic diagram summarizing the average particle pathway from solution to crystal for calcium carbonate, as observed in this work.

This is broadly in line with previous observations, for example: the precipitation of ACC particles of 35–40 nm [5], the observation of 100 nm particles in amorphous and crystal phases [42,45], 50–60 nm crystals [46], and 100 nm silica-coated ACC particles with 20% water [47]. Electron microscopy [48] as revealed the evolution of particles prior to step 1 above, with ACC particles growing from ~1 nm to ~20 nm in a range of a few seconds. Prenucleation clusters of size ~1 nm are thought to precede the nanoparticles of ~30 nm [49].

Values of the rates for step R_1 were found to be largely independent of Mg/Ca ratio while the Mg/Ca ratio had a very large effect on the rates for steps R_2 and R_3 . The change in rate for steps R_2 and R_3 with Mg/Ca ratio were found to be very similar. From a classical nucleation and growth perspective this might imply that the addition of magnesium mainly effects particle growth and has little effect on nucleation. This might explain why biomineralization predominantly involves nanoparticles since the nucleation rate is largely unregulated while the growth rate can be controlled.

All ACC samples were found to contain magnesium, but all the crystalline aragonite products were found not to contain any magnesium. The high rate for crystallisation observed suggests that this process does not involve diffusion in the solid state. This suggests that our results would favour a dissolution and reprecipitation model for ACC transformation to aragonite over a solid-state transformation model.

In this case, the nanoparticles were found to not simply orientate and attach to form larger structures but to dissolve and recrystallize as part of the self-assembly process. The bigger question we then ask is to what extent is this mechanism employed in self-assembly for both biological and synthetic systems.

Supplementary Materials: The following supporting information can be downloaded at: <https://www.mdpi.com/article/10.3390/nano12234151/s1>. Figure S1. Typical TGA pattern of an ACC sample. Figure S2. X-ray powder diffraction pattern of our Mg-ACC sample with two diffuse maxima. Figure S3. X-ray scattering of solid-solution mixtures of $(\text{Ca}_{1-x}\text{Mg}_x)\text{CO}_3$. Figure S4. Neutron scattering patterns of samples prepared with different Mg/Ca ratios. Figure S5. Neutron scattering data of $\text{H}_2\text{O}/\text{D}_2\text{O}$ mixtures. Figure S6. Representative Raman spectrum. Figure S7. X-ray powder diffraction pattern of an ACC converted into aragonite. Figure S8. SEM micrograph of a synthesised sample from this study showing tablets of aragonite and xenomorphic aggregates believed to be ACC. Figure S9. SANS patterns evolving with time. Figure S10. XRD patterns during crystallization of aragonite from ACC. Table S1. Water content and Mg/Ca ratios determined for ACC.

Author Contributions: S.M.C. devised the project, assisted with data collection, processing and interpretation and wrote the manuscript. V.G. contributed to preparation of the manuscript. B.C. synthesised the samples, carried out sample characterisation, measured the neutron and X-ray data, analysed the bulk of the data and prepared the first draft of this manuscript. T.A.D. helped devise the synthesis protocols and oversaw the synthesis procedures. K.W. oversaw the SANS data collection and processing. J.N. oversaw the neutron scattering data collection and processing on NOMAD. D.E.J. helped devise the project and contributed to data interpretation and manuscript preparation. All authors have read and agreed to the published version of the manuscript.

Funding: We would like to thank the Australian Centre for Neutron Scattering for the award of neutron beamtime on QUOKKA under proposals number NDF3219 and NDF2769. Thanks also to the Oak Ridge National Laboratory for provision of beam time on the NOMAD instrument under proposal number IPTS-17259.1.

Data Availability Statement: All data is available on request from the corresponding author.

Acknowledgments: We thank colleagues at the Department of Earth and Environmental Sciences at Macquarie University for technical support and fruitful discussions, specifically we are grateful to Russell Field, Will Powell and Norman Pearson. LA-ICPMS data were obtained using instrumentation funded by DEST Systemic Infrastructure Grants, ARC LIEF, NCRIS/AuScope, industry partners and Macquarie University. Aragonite and calcite reference samples were made available from the mineral collection of the Department of Earth and Planetary Sciences at Macquarie University. We thank the Australian Centre for Neutron Scattering for provision of beamtime on QUOKKA and Oak Ridge National Laboratory for provision of beam time on NOMAD. SMC and BC would like to acknowledge partial financial support from the Australian Nuclear Science and Technology Organization. DEJ acknowledges support from the Australian Research Council (DP210101268). We thank Andrew Whitten for assistance with measurements on QUOKKA. The National Deuteration Facility is partly supported by the National Collaborative Research Infrastructure Strategy an initiative of the Australian Government.

Conflicts of Interest: The authors declare no conflict of interest.

References

1. Politi, Y.; Metzler, R.A.; Abrecht, M.; Gilbert, B.; Wilt, F.H.; Sagi, I.; Addadi, L.; Weiner, S.; Gilbert, P.U.P.A. Transformation mechanism of amorphous calcium carbonate into calcite in the sea urchin larval spicule. *Proc. Natl. Acad. Sci. USA* **2008**, *105*, 17362–17366. [[CrossRef](#)]
2. Navrotsky, A. Energetic clues to pathways to biomineralization: Precursors, clusters, and nanoparticles. *Proc. Natl. Acad. Sci. USA* **2004**, *101*, 12096–12101. [[CrossRef](#)]
3. De Yoreo, J.J.; Gilbert, P.U.P.A.; Sommerdijk, N.A.; Penn, R.L.; Whitlam, S.; Joester, D.; Zhang, H.; Rimer, J.D.; Navrotsky, A.; Banfield, J.F. Crystallisation by particle attachment in synthetic, biogenic, and geologic environments. *Science* **2015**, *349*, aaa6760. [[CrossRef](#)]
4. Cartwright, J.H.E.; Checa, A.G.; Gale, J.D.; Gebauer, D.; Sainz-Días, C.I. Calcium carbonate polyamorphism and its role in biomineralisation: How many amorphous calcium carbonates are there? *Angew. Chem. Int. Ed.* **2012**, *51*, 11960–11970. [[CrossRef](#)] [[PubMed](#)]
5. Bots, P.; Benning, L.G.; Rodriguez-Blanco, J.-D.; Roncal-Herrero, T.; Shaw, S. Mechanistic Insights into the Crystallization of Amorphous Calcium Carbonate (ACC). *Cryst. Growth Des.* **2012**, *12*, 3806–3814. [[CrossRef](#)]
6. Clark, S.M.; Colas, B.; Jacob, D.E.; Neufeind, J.C.; Wang, H.-W.; Page, K.L.; Soper, A.K.; Schodder, P.I.; Duchstein, P.; Zubiri, B.A.; et al. The nano- and meso-scale structure of amorphous calcium carbonate indicate nanoscale assembly processes. *Sci. Rep.* **2022**, *12*, 6870. [[CrossRef](#)]

7. Rodriguez-Blanco, J.D.; Shaw, S.; Benning, L.G. The kinetics and mechanisms of amorphous calcium carbonate (ACC) crystallization to calcite, via vaterite. *Nanoscale* **2011**, *3*, 265–271. [[CrossRef](#)] [[PubMed](#)]
8. Stephens, C.J.; Ladden, S.F.; Meldrum, F.C.; Christenson, H.K. Amorphous Calcium Carbonate is Stabilized in Confinement. *Adv. Funct. Mater.* **2010**, *20*, 2108–2115. [[CrossRef](#)]
9. Addadi, L.; Raz, S.; Weiner, S. Taking Advantage of Disorder: Amorphous Calcium Carbonate and Its Roles in Biomineralization. *Adv. Mater.* **2003**, *15*, 959–970. [[CrossRef](#)]
10. Ouhenia, S.; Chateigner, D.; Belkhir, M.; Guilmeau, E.; Krauss, C. Synthesis of calcium carbonate polymorphs in the presence of polyacrylic acid. *J. Cryst. Growth* **2008**, *310*, 2832–2841. [[CrossRef](#)]
11. Huang, S.-C.; Naka, K.; Chujo, Y. A Carbonate Controlled-Addition Method for Amorphous Calcium Carbonate Spheres Stabilized by Poly(acrylic acid)s. *Langmuir* **2007**, *23*, 12086–12095. [[CrossRef](#)] [[PubMed](#)]
12. Lam, R.S.K.; Charnock, J.M.; Lennie, A.; Meldrum, F.C. Synthesis-dependant structural variations in amorphous calcium carbonate. *CrystEngComm* **2007**, *9*, 1226–1236. [[CrossRef](#)]
13. Loste, E.; Wilson, R.M.; Seshadri, R.; Meldrum, F.C. The role of magnesium in stabilising amorphous calcium carbonate and controlling calcite morphologies. *J. Cryst. Growth* **2003**, *254*, 206–218. [[CrossRef](#)]
14. Rodriguez-Blanco, J.; Shaw, S.; Bots, P.; Roncal-Herrero, T.; Benning, L. The role of pH and Mg on the stability and crystallization of amorphous calcium carbonate. *J. Alloys Compd.* **2011**, *536*, S477–S479. [[CrossRef](#)]
15. Foran, E.; Weiner, S.; Fine, M. Biogenic Fish-gut Calcium Carbonate is a Stable Amorphous Phase in the Gilt-head Seabream, *Sparus aurata*. *Sci. Rep.* **2013**, *3*, 1700–1705. [[CrossRef](#)]
16. Pai, R.K.; Pillai, S. Nanoparticles of amorphous calcium carbonate by miniemulsion: Synthesis and mechanism. *CrystEngComm* **2008**, *10*, 865–872. [[CrossRef](#)]
17. Sun, W.; Jayaraman, S.; Chen, W.; Persson, K.A.; Ceder, G. Nucleation of metastable aragonite CaCO₃ in seawater. *Proc. Natl. Acad. Sci. USA* **2015**, *112*, 3199–3204. [[CrossRef](#)]
18. Zhang, Z.; Xie, Y.; Xu, X.; Pan, H.; Tang, R. Transformation of amorphous calcium carbonate into aragonite. *J. Cryst. Growth* **2012**, *343*, 62–67. [[CrossRef](#)]
19. Blue, C.; Dove, P. Chemical controls on the magnesium content of amorphous calcium carbonate. *Geochim. Cosmochim. Acta* **2015**, *148*, 23–33. [[CrossRef](#)]
20. Gal, A.; Habraken, W.; Gur, D.; Fratzl, P.; Weiner, S.; Addadi, L. Calcite Crystal Growth by a Solid-State Transformation of Stabilized Amorphous Calcium Carbonate Nanospheres in a Hydrogel. *Angew. Chem. Int. Ed.* **2013**, *52*, 4867–4870. [[CrossRef](#)]
21. Ihli, J.; Kim, Y.-Y.; Noel, E.H.; Meldrum, F.C. The Effect of Additives on Amorphous Calcium Carbonate (ACC): Janus Behavior in Solution and the Solid State. *Adv. Funct. Mater.* **2012**, *23*, 1575–1585. [[CrossRef](#)]
22. Pontoni, D.; Bolze, J.; Dingenouts, N.; Narayanan, T.; Ballauff, M. Crystallization of Calcium Carbonate Observed In-situ by Combined Small- and Wide-angle X-ray Scattering. *J. Phys. Chem. B* **2003**, *107*, 5123–5125. [[CrossRef](#)]
23. Giuffre, A.J.; Gagnon, A.C.; De Yoreo, J.J.; Dove, P.M. Isotopic tracer evidence for the amorphous calcium carbonate to calcite transformation by dissolution–reprecipitation. *Geochim. Cosmochim. Acta* **2015**, *165*, 407–417. [[CrossRef](#)]
24. Liu, Z.; Zhang, Z.; Wang, Z.; Jin, B.; Li, D.; Tao, J.; Tang, R.; De Yoreo, J.J. Shape-preserving amorphous-to-crystalline transformation of CaCO₃ revealed by in situ TEM. *Proc. Natl. Acad. Sci. USA* **2020**, *117*, 3397–3404. [[CrossRef](#)] [[PubMed](#)]
25. Jacob, D.E.; Wirth, R.; Agbaje, O.B.A.; Branson, O.; Eggins, S.M. Planktic foraminifera form their shells via metastable carbonate phases. *Nat. Commun.* **2017**, *8*, 1265. [[CrossRef](#)]
26. Nielsen, M.H.; Aloni, S.; De Yoreo, J.J. In situ TEM imaging of CaCO₃ nucleation reveals coexistence of direct and indirect pathways. *Science* **2014**, *345*, 1158–1162. [[CrossRef](#)] [[PubMed](#)]
27. Fernandez-Martinez, A.; Kalkan, B.; Clark, S.M.; Waychunas, G.A. Pressure-Induced Polyamorphism and Formation of ‘Aragonitic’ Amorphous Calcium Carbonate. *Angew. Chem. Int. Ed.* **2013**, *52*, 8354–8357. [[CrossRef](#)]
28. Jochum, K.P.; Nohl, U.; Herwig, K.; Lammel, E.; Stoll, B.; Hofmann, A.W. GeoReM: A new geochemical database for reference materials and standards. *Geostand. Geoanal. Res.* **2006**, *29*, 333–338. [[CrossRef](#)]
29. Doebelin, N.; Kleeberg, R. Profex: A graphical user interface for the Rietveld refinement program BGMN. *J. Appl. Crystallogr.* **2015**, *48*, 1573–1580. [[CrossRef](#)]
30. Radha, A.; Fernandez-Martinez, A.; Hu, Y.; Jun, Y.-S.; Waychunas, G.A.; Navrotsky, A. Energetic and structural studies of amorphous Ca_{1-x}Mg_xCO₃·nH₂O (0 ≤ x ≤ 1). *Geochim. Cosmochim. Acta* **2012**, *90*, 83–95. [[CrossRef](#)]
31. Wood, K.; Mata, J.; Garvey, C.J.; Wu, C.-M.; Hamilton, W.A.; Abbeywick, P.; Bartlett, D.; Bartsch, F.; Baxter, P.; Booth, N.; et al. QUOKKA, the pinhole small-angle neutron scattering instrument at the OPAL Research Reactor, Australia: Design, performance, operation and scientific highlights. *J. Appl. Crystallogr.* **2018**, *51*, 294–314. [[CrossRef](#)]
32. Wang, D.; Hamm, L.M.; Giuffre, A.J.; Echigo, T.; Rimstidt, J.D.; De Yoreo, J.J.; Grotzinger, J.; Dove, P.M. Revisiting geochemical controls on patterns of carbonate deposition through the lens of multiple pathways to mineralization. *Faraday Discuss.* **2012**, *159*, 371–386. [[CrossRef](#)]
33. Xu, J.; Yan, C.; Zhang, F.; Konishi, H.; Xu, H.; Teng, H.H. Testing the cation-hydration effect on the crystallization of Ca–Mg–CO₃ systems. *Proc. Natl. Acad. Sci. USA* **2013**, *110*, 17750–17755. [[CrossRef](#)]
34. Wang, Y.-W.; Kim, Y.-Y.; Stephens, C.J.; Meldrum, F.C.; Christenson, H.K. In Situ Study of the Precipitation and Crystallization of Amorphous Calcium Carbonate (ACC). *Cryst. Growth Des.* **2012**, *12*, 1212–1217. [[CrossRef](#)]

35. Parker, J.E.; Thompson, S.P.; Lennie, A.R.; Potter, J.; Tang, C.C. A study of the aragonite-calcite transformation using Raman spectroscopy, synchrotron powder diffraction and scanning electron microscopy. *CrystEngComm* **2010**, *12*, 1590–1599. [[CrossRef](#)]
36. Wehrmeister, U.; Jacob, D.E.; Soldati, A.L.; Loges, N.; Häger, T.; Hofmeister, W. Amorphous, nanocrystalline and crystalline calcium carbonates in biological materials. *J. Raman Spectrosc.* **2010**, *42*, 926–935. [[CrossRef](#)]
37. Lafuente, B.; Downs, R.T.; Yang, H.; Stone, N. 1. The Power of Databases: The RRUFF Project. In *Highlights in Mineralogical Crystallography*; Armbruster, T., Danisi, R.M., Eds.; De Gruyter: Berlin, Germany, 2016; pp. 1–30. ISBN 9783110417104.
38. Nudelman, F. Nacre biomineralisation: A review on the mechanisms of crystal nucleation. *Semin. Cell Dev. Biol.* **2015**, *46*, 2–10. [[CrossRef](#)] [[PubMed](#)]
39. Dudnikova, V.B.; Eremin, N.N. Simulation of the local structure, properties of mixing, and stability of solid solutions $Ba_x Sr_{1-x} CO_3$ by the interatomic potential method. *Phys. Solid State* **2016**, *58*, 1101–1107. [[CrossRef](#)]
40. Stuhmann, H. Small-angle scattering of X-rays. *Prog. Cryst. Growth Charact.* **1989**, *18*, 1–19. [[CrossRef](#)]
41. Jacob, D.; Wirth, R.; Soldati, A.; Wehrmeister, U.; Schreiber, A. Amorphous calcium carbonate in the shells of adult Unionoida. *J. Struct. Biol.* **2011**, *173*, 241–249. [[CrossRef](#)]
42. Wolf, S.E.; Böhm, C.; Harris, J.; Hajir, M.; Mondeshki, M.; Marin, F. Single Nanogranules Preserve Intracrystalline Amorphicity in Biominerals. *Key Eng. Mater.* **2016**, *672*, 47–59. [[CrossRef](#)]
43. Nassif, N.; Pinna, N.; Gehrke, N.; Antonietti, M.; Jäger, C.; Cölfen, H. Amorphous layer around aragonite platelets in nacre. *Proc. Natl. Acad. Sci. USA* **2005**, *102*, 12653–12655. [[CrossRef](#)] [[PubMed](#)]
44. Macías-Sánchez, E.; Willinger, M.G.; Pina, C.M.; Checa, A.G. Transformation of ACC into aragonite and the origin of the nanogranular structure of nacre. *Sci. Rep.* **2017**, *7*, 12728. [[CrossRef](#)] [[PubMed](#)]
45. Jacob, D.; Soldati, A.; Wirth, R.; Huth, J.; Wehrmeister, U.; Hofmeister, W. Nanostructure, composition and mechanisms of bivalve shell growth. *Geochim. Cosmochim. Acta* **2008**, *72*, 5401–5415. [[CrossRef](#)]
46. Hovden, R.; Wolf, S.E.; Holtz, M.E.; Marin, F.; Muller, D.A.; Estroff, L.A. Nanoscale assembly processes revealed in the nacre-prismatic transition zone of *Pinna nobilis* mollusc shells. *Nat. Commun.* **2015**, *6*, 10097. [[CrossRef](#)]
47. Ihli, J.; Wong, W.C.; Noel, E.H.; Kim, Y.-Y.; Kulak, A.N.; Christenson, H.K.; Duer, M.J.; Meldrum, F.C. Dehydration and crystallization of amorphous calcium carbonate in solution and in air. *Nat. Commun.* **2014**, *5*, 3169. [[CrossRef](#)] [[PubMed](#)]
48. Smeets, P.J.M.; Cho, K.R.; Kempen, R.G.E.; Sommerdijk, N.A.J.M.; De Yoreo, J.J. Calcium carbonate nucleation driven by ion binding in a biomimetic matrix revealed by in situ electron microscopy. *Nat. Mater.* **2015**, *14*, 394–399. [[CrossRef](#)]
49. Pouget, E.M.; Bomans, P.H.H.; Goos, J.A.C.M.; Frederik, P.M.; de With, G.; Sommerdijk, N.A.J.M. The Initial Stages of Template-Controlled $CaCO_3$ Formation Revealed by Cryo-TEM. *Science* **2009**, *323*, 1455–1458. [[CrossRef](#)]